Hindawi
Journal of Nanomaterials
Volume 2023, Article ID 2856806, 9 pages
https://doi.org/10.1155/2023/2856806

Research Article

Effects of Different Precursors on Particle Size and Optical–Magnetic Properties of $ZnCr_2O_4$ Nanoparticles Prepared by Microwave-Assisted Method

P. Sankudevan,[1] R. V. Sakthivel,[1] K. Poonkodi,[2] Gopal Ramalingam,[3] C. Raghupathi,[4] Mohammed Mujahid Alam,[5] and Baskaran Rangasamy[6]

[1]*Department of Chemistry, Arignar Anna Government Arts College, Namakkal 637 402, Tamil Nadu, India*
[2]*Department of Chemistry, Nallamuthu Gounder Mahalingam College, Pollachi, Coimbatore 642005, Tamil Nadu, India*
[3]*Department of Nanoscience and Technology, Alagappa University, Karaikudi 630003, India*
[4]*Department of Chemistry, Sriram College of Arts and Science, Thiruvallur 602024, India*
[5]*Department of Chemistry, College of Science, King Khalid University, PO Box 9004, Abha 61413, Saudi Arabia*
[6]*Energy Storage Materials and Devices Lab, Department of Physics, School of Mathematics and Natural Sciences, The Copperbelt University, PO Box 21692, Riverside, Jambo Drive, Kitwe 10101, Zambia*

Correspondence should be addressed to R. V. Sakthivel; velsakthi1123@gmail.com, Gopal Ramalingam; ramanloyola@gmail.com and Baskaran Rangasamy; baskaran.rangasamy@cbu.ac.zm

Received 17 July 2022; Revised 21 November 2022; Accepted 24 November 2022; Published 7 January 2023

Academic Editor: Zehra Durmus

Zinc chromite ($ZnCr_2O_4$)-based nanoparticles have various exceptional properties that make them suitable for use in a variety of fields, including chemistry, medicine, energy, the environment, industry, and information. In this work, nanocrystalline $ZnCr_2O_4$ has been effectively synthesized with a distinct fuel by microwave-assisted solution combustion method. The XRD results reveal a single-phase high pure formation of nanoscale $ZnCr_2O_4$. The $ZnCr_2O_4$ samples are further characterized by scanning electron microscopy, transmission electron microscope, UV–Vis absorption spectroscopy, and vibrating sample magnetometer. The results reveal that modifying the fuel precursors in the combustion technique played an impact on the particle size, bandgap energy, magnetic properties, and reaction time of the $ZnCr_2O_4$ preparation. The average particle size of the various samples ranged from 18.6 to 13.9 nm with various fuels. The significance of this study is the tuning effect of optical and magnetic properties of $ZnCr_2O_4$ by using various fuel precursors.

1. Introduction

During the last decade, the solution combustion synthesis technology had been used to investigate the effect of the chemical nature of chain of five fuel molecules (urea, succinic acid, citric acid, maleic acid, and glycine) on the combustion reaction mechanism, physical and chemical properties of synthesized samples. The one-step exothermic process used in Type I contains citric acid, urea, succinic acid, glycine, and maleic acid which produced NO_2 and semidecomposed mixed nitrate–fuel complex by metal nitrate decomposition. The temperature needed to effectively synthesize and crystallize metal oxide particles may be obtained due to the combustion heat emission. Type II was characterized by a multistage process that included intermediate breakdown processes prior to the production of a mixed nitrate −fuel complex. In a nutshell, solution combustion synthesis method is efficient to produce nanomaterials, which is based on a self-sustaining combustion reaction in aqueous media between an oxidant (nitrate) and a sacrificial organic molecule utilized as fuel [1, 2].

Nanostructured material properties often vary greatly from those of bulk materials by which innovative materials are developed for modern applications, such as optical, catalysis, magnetic, spintronics, data storage, telecommunications, and biomedicine [3–5]. As a result, the crystal size,

structure, morphology, and surface area of oxide semiconductors may play an essential role in determining the optical characteristics. Spinel oxides have drawn keen interest among the scientific community due to their distinctive structure, shape, and characteristics. When scaled down to the nanoscale, the spinel oxides have a significant impact on both the physical and chemical properties [6]. It is now well accepted that any modification of controlled shape may significantly affect the chemical and physical properties of metal oxides. In this sense, doping rare earth metals with different transition metals is a frequent practice to tune the optical and magnetic properties [7]. Despite extensive study on nanostructured oxides, it is still a challenging task to create excellent crystalline oxides with remarkable properties.

Many researchers reported the synthesis of manganese oxides by using a variety of techniques, such as combustion, thermal decomposition, solvothermal, microwave, sol–gel, hydrothermal, and coprecipitation processes [7–9]. In comparison to other approaches, the microwave process has the benefits of high stoichiometric ratio control, superior homogeneousness, the ability to produce powders and thin films of nanomaterials, and lower handling temperatures [9]. Among the synthesis methods, a most affordable, quick, and low-energy soft technique for the synthesis of simple and mixed oxide compounds is combustion reaction [6]. High-surface and evenly dispersed oxide nanoparticles are produced by the thermally induced redox reaction between a fuel (F, an organic molecule that begins the process) and an oxidant (O, typically nitrate anions). The temperature of the flame and the whole combustion mechanism are affected by the F/O ratio of fuel and thermochemical characteristics [10]. The microwave combustion method has the advantage of resulting in a high exothermic reaction, which causes the production of spherical particles to occur immediately. The uniform temperature distribution caused by microwave heat treatment allows for the quick formation of nanoparticles in both the surface and bulk material. Chemical processes may now be accelerated in a microwave system more quickly than with the conventional method due to microwave dielectric heating. Furthermore, microwave irradiation achieves a high reaction temperature, resulting in an increase in the chemical reaction speed as well as controlled spherical shapes [11–14].

In this work, a novel single-fuel combustion-based synthesis of $ZnCr_2O_4$ powders by utilizing citric acid, urea, succinic acid, glycine, and maleic acid has been demonstrated. The structural, morphology, and composition analyses have been performed to confirm the physical characteristics of the nano $ZnCr_2O_4$. The UV–visible and VSM investigations have been carried out to reveal the optical and magnetic properties of the zinc chromite, respectively. The impact of fuel nature and F/O ratio on crystallite size, morphology, and optical–magnetic characteristics has been discussed.

2. Experimental Details

2.1. Synthesis of Nano $ZnCr_2O_4$. Nanoscale $ZnCr_2O_4$ samples have been synthesized by self-sustaining combustion reaction route in aqueous media with an oxidant (nitrate) and fuels of sacrificial organic molecule. Initially, the two salt solutions, zinc(II) nitrate hexahydrate and potassium dichromate, each with 0.6 M are combined together in distilled water. Subsequently, a dropwise introduction of 6.0 ml of anyone of the single fuel such as citric acid (CA), succinic acid (SA), maleic acid (MA), glycine (G), and urea (U) in a solution (0.8 M) is added to the aforesaid mixture separately for synthesizing each of the $ZnCr_2O_4$ compounds. The obtained solution is kept in a microwave oven (2,450 MHz operating frequency and 1,500 W power), and microwave treatment is applied for 18 min. The abovementioned homogeneous mixture begins to boil rapidly and releases gases such as N_2, NH_3, O_2, and CO_2 in the combustion reaction during the microwave irradiation. The liquid vaporizes and solidifies when the chemical source combination reaches a spontaneous combustion state. The resultant solid substance is effectively cleaned with ethanol before being evaporated at 180°C for 1 hr. The $ZnCr_2O_4$ samples synthesized with different fuels are named as glycine (a), maleic acid (b), succinic acid (c), citric acid (d), and urea (e), respectively.

2.2. Characterization. X-ray diffraction patterns of $ZnCr_2O_4$ nanomaterial are analyzed using an X-ray diffractometer (Rigaku) by using Cu Kα radiation source. The morphology and elemental composition are determined by scanning electron microscopic (SEM) images. A high-resolution transmission electron microscope (HR-TEM) (Philips EM 208) with a 200 kV accelerating voltage is used to observe the particle size and morphology at higher magnifications. For morphological observations and energy-dispersive X-ray investigations of nanomaterials, a Joel JSM6360 high-resolution scanning electron microscope is employed. The samples are coated with gold using gold spraying equipment to increase the clarity of the surface morphology. The Cary 100 UV–visible spectrophotometer is used to capture the diffuse reflectance UV–visible spectra of the $ZnCr_2O_4$ nanomaterials. Magnetic measurements are performed at room temperature with a PMC Micro Mag 3900 model vibrating sample magnetometer (VSM) outfitted with a 1 T magnet.

3. Results and Discussion

3.1. XRD Analysis. Figure 1(a)–1(e) depicts typical XRD patterns of as-prepared nanoscale $ZnCr_2O_4$ powder samples synthesized with each of the fuels glycine, maleic acid, succinic acid, citric acid, and urea. The XRD pattern indicates peaks at different 2θ positions corresponding to crystalline planes (111), (220), (311), (222), (400), (422), (511), (440), and (533), which are attributed to single-phase formation of $ZnCr_2O_4$. The obtained results are well harmonized with standard JCPDS card no. 22-1107. The XRD pattern shows high pure $ZnCr_2O_4$ powder sample formation due to the nonexistence of any additional phases. The XRD pattern shows a minor displacement of the peak locations of the $ZnCr_2O_4$ powders in the direction of greater angles, indicating a little distortion of the system symmetry caused by the formation of defects and vacancies.

The crystallite size of $ZnCr_2O_4$ decreases for different fuels because of the increase in full width at half maximum

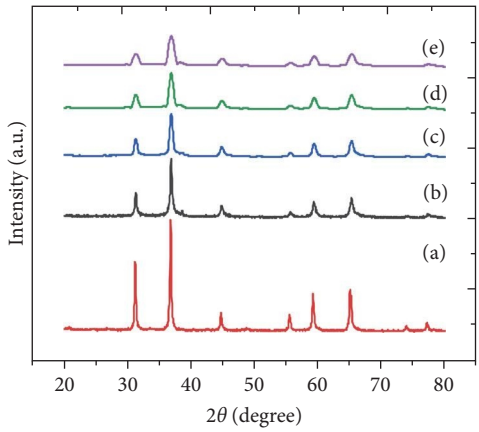

FIGURE 1: XRD pattern of nano $ZnCr_2O_4$ synthesized by using different fuel precursors: (a) glycine, (b) maleic acid, (c) succinic acid, (d) citric acid, and (e) urea.

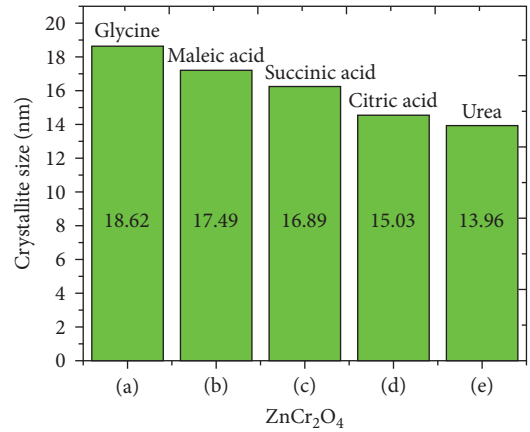

FIGURE 2: Crystallite size variations of nano $ZnCr_2O_4$ synthesized by using different fuel precursors: (a) glycine, (b) maleic acid, (c) succinic acid, (d) citric acid, and (e) urea.

(FWHM) value [15, 16]. The mean crystal dimension is calculated from the peak intensity [17] by applying the Debye–Scherrer formula:

$$L = \frac{0.89\,\lambda}{\beta \cos\theta}, \tag{1}$$

where L denotes the mean crystallite dimension (Å) and λ is the X-ray beam incident wavelength (1.54 Å). The Bragg's angle is mentioned by θ and the FWHM (radian) is denoted by β.

As shown in Figure 2, the crystallite dimension for the synthesized $ZnCr_2O_4$ nanoparticles by using different fuels varies from 18.62 to 13.96 nm for glycine to urea, respectively. Furthermore, the fine lines as well as displacement line intensity both exhibit the similar orientation, suggesting that the defect is becoming less severe. The d_{XRD} is the mean of diameter of the coherently scattering domain, which is expected to be spherical. The lattice parameter is disproportionally biased toward a smaller particle size in the nonmonodispersed samples.

Despite the fact that the average volume is not a precisely determined number for a multidispersion system, which is affected by the weighting technique utilized. The XRD intensity is weighted by the square of the crystal sizes. Furthermore, in nonmonodispersive samples, XRD peak is significantly skewed toward bigger particle size [18]. Table 1 shows the lattice parameter, cell volume, and observed crystallite size values estimated from XRD data for $ZnCr_2O_4$ nanoparticles synthesized with various fuels.

3.2. Morphology Analysis. Figure 3 shows SEM surface morphology and higher magnified TEM images of $ZnCr_2O_4$ samples synthesized by using various fuels. The SEM morphology demonstrates spherulite particle morphology. The majority of the particles are of hexagonal form. The morphology demonstrates nanoparticles with uneven form. Agglomeration occurs among the particles, possibly as a result of dipole–dipole interaction among the particles. The grain size of the as-synthesized samples is assessed using a method of line intercepts that indicates grain sizes located between 21 and 16 nm. In order to reveal clear particle morphology, high-resolution TEM morphology observations are made. It is interesting to observe uniform particle distributions with distinct grain boundaries in TEM images. Furthermore, the particles aggregate in a chain-like fashion, and each particle has a structure of ball-shaped granular.

The particle sizes of $ZnCr_2O_4$, synthesized with different fuels as mentioned above, determined from SEM and TEM observations are given in Table 2. However, because of the agglomeration of nanoparticles in all five samples, the calculation of the size distribution is fairly imprecise. The secondary aggregated size of the generated particles is reported to be in the range of 20–30 nm, with an uneven form. A schematic representation shows a formation of regular nanoparticles by microwave-assisted method and agglomerated nanoparticles on storage (Figure 4). The synthesized $ZnCr_2O_4$ particles by the microwave-assisted method are of irregular polyhedron shapes with 10–20 nm. All five samples of $ZnCr_2O_4$ synthesized by using the microwave-assisted technique are found to have uneven polyhedron forms and different particle sizes ranging in the range of several hundred nanometers. As a result, a fuel combination of flame fuels is an appropriate option for controlling the flame temperature, as well as the size distribution, surface area, and agglomeration degree of the end product's particles.

The oxygen atoms in wurtzite are organized in a hexagonal tight packing, with zinc atoms filling half of the tetrahedral positions. Zn and O atoms are tetrahedrally coordinated and, hence, they occupy an analogous location. The Zn structure is open, with all octahedral sites and half of the tetrahedral sites unfilled. The observed disparity in particle size measured by XRD and HR-TEM/SEM (Table 2) might be attributable to molecular structural defects and lattice strain caused by differing ionic radii and/or clustering of the nanoparticles. As a result, the XRD technique is more standard and produces smaller particle sizes [19, 20].

Table 1: Characteristic data of different nano $ZnCr_2O_4$ samples obtained from XRD.

Fuels	Crystallite size of $ZnCr_2O_4$ (nm)	Lattice parameter (Å)	Cell volume (Å^3)
Glycine (a)	±18.33	±5.41	±158.44
Maleic acid (b)	±16.03	±5.42	±159.34
Succinic acid (c)	±15.21	±5.44	±162.04
Citric acid (d)	±14.93	±5.45	±164.44
Urea (e)	±14.03	±5.46	±165.59

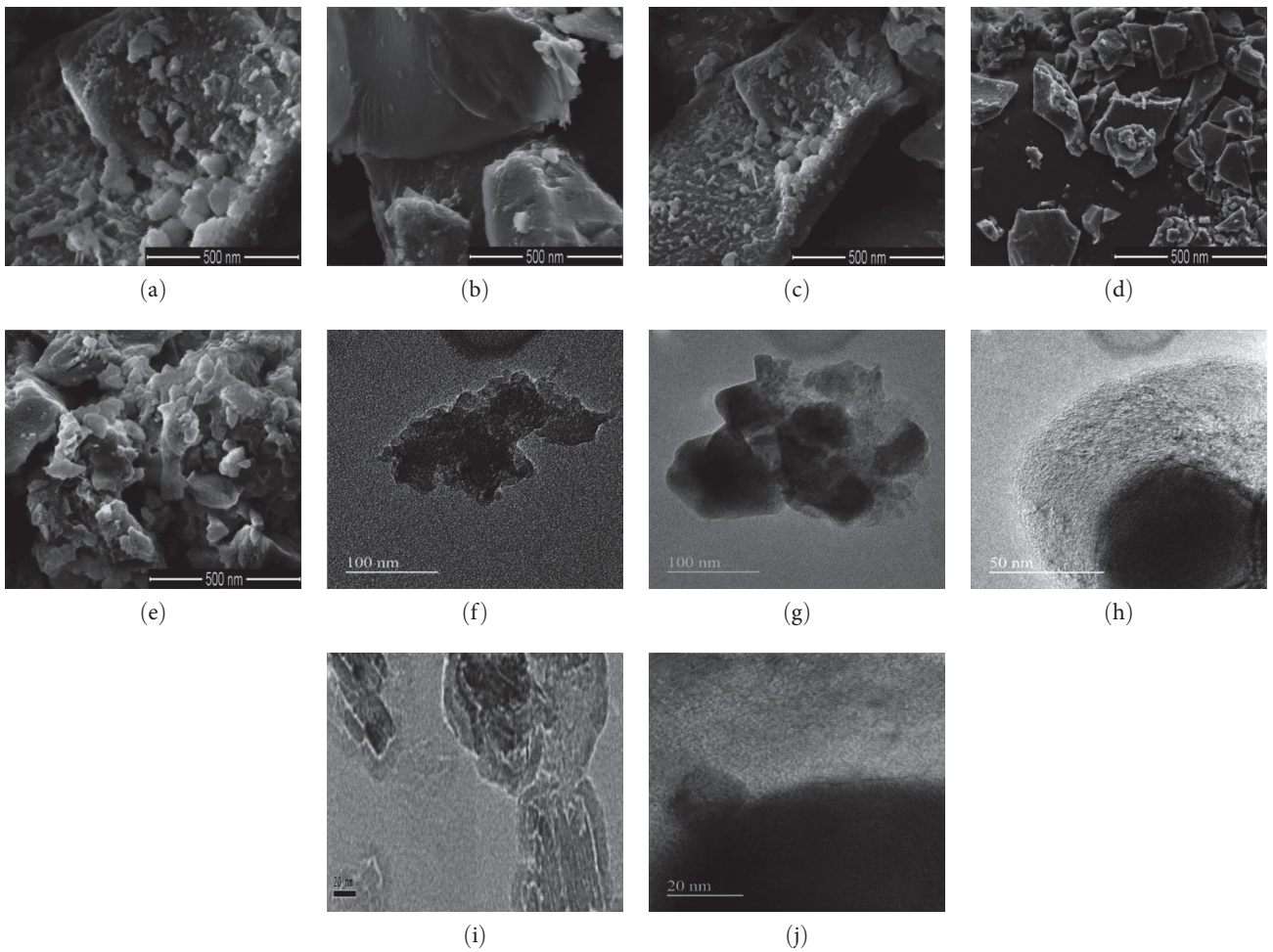

Figure 3: SEM morphology (a–e) and TEM images (f–j) of $ZnCr_2O_4$ nanoscale materials synthesized with various fuels.

3.3. Bandgap Energy Investigation. In solid-state physics, the bandgap of a semiconductor is the distance between an electron-filled valence band and a completely empty conduction band (CB). The Kubelka–Munk model is used to calculate the bandgap energy (E_g) [21]. It is evident that as the Cr concentration increases, the E_g value varies from 1.46 to 2.22 eV, as shown in Figure 5. The increased bandgap energy might be due to the creation of energy levels and interface defects [22]. The study of bandgap energy is a fundamental optical characteristic that gives an adequate tool for analyzing semiconductors. Furthermore, the *sp–d* spin exchange interaction among the spin of the band electrons of $ZnCr_2O_4$ (five samples), in other words, the conduction and valence bands, and the spin of the Zn and Cr *d* orbitals, as well as the Burstein–Moss (BM) impact, might be contributed to the increase of bandgap [23, 24]. The BM effect is commonly used for semiconductors having contents wherein the density of electron carriers surpasses the density of states present at the CB edge [25]. This pattern could be ascribed to positive and negative variations in the valence and CBs caused by changes in the *sp–d* exchange interactions among the band electrons and the localized *d* electrons of the Zn^{2+} and Cr^{3+} ions, respectively [26]. Due to the quantum confinement of $ZnCr_2O_4$ nanoparticles, bandgap increases when particle size is reduced. Electron energy levels in nanoscale materials are changed from continuous to discontinuous states. The energy difference between the free electron and location of the CB causes quantization of their energy levels.

Table 2: Crystallite sizes of $ZnCr_2O_4$ determined from XRD, SEM, and TEM measurements.

Fuels used for synthesis of $ZnCr_2O_4$	Crystallite size by XRD (nm)	Particle size by SEM (nm)	Particle size by TEM (nm)
Glycine (a)	±18.33	±17.03	±16.21
Maleic acid (b)	±16.03	±16.21	±15.78
Succinic acid (c)	±15.21	±15.03	±14.90
Citric acid (d)	±14.93	±14.56	±13.33
Urea (e)	±14.03	±13.12	±12.56

d_{XRD} is disproportionally biased toward a smaller particle size in the nonmonodispersed samples. In addition, the nanoparticles of $ZnCr_2O_4$ are strongly agglomerated in the TEM/SEM specimen-support film and, therefore, the estimation of the size distribution is rather rough. The small differences are inherent to the calculation or measuring errors.

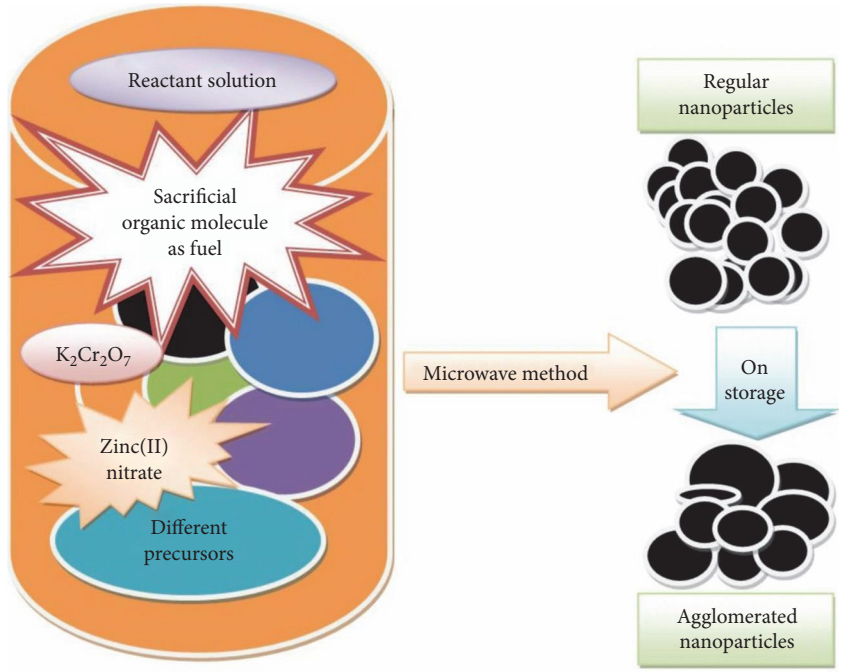

Figure 4: Schematic representation of the $ZnCr_2O_4$ particle nature depending on the type of the different fuels.

When particle size decreases, the energy levels reach highly distinct atomic levels.

As already noted, defects may be produced within crystalline and noncrystalline materials through a variety of physical processes of the defects' energy level inside the host's bandgap. Generally, the level locations of the defects with regard to the bottom of the CB vary according to the origin of the faults and the hosts types (Figure 6). On the other hand, the introduction of metal oxides into the host lattice frequently causes a shift in the trap depth with regard to the VB–CB. E_{gap} investigations are crucial regarding optical properties, vacancies, and crystalline flaws in the long, medium, and short ranges of crystalline compositions [27]. Any localized irregularity in the O–Cr–O or O–Zn–O bond angles or lengths caused by local stress or edge and interface misrepresentation is enough to break the cluster symmetry, which results change in the bandgap. When the local disorder exists prior to light radiation, polaronic deformation is facilitated, and the material would exhibit flawless single crystal. As the exponential optical absorption edge and E_{gap} are regulated by the degree of structural order–disorder in the lattice, it is believed that this behavior is connected to the development of intermediary energy levels between the CB and VB (Figure 7). In the first example, the nanostructure may change the symmetry of the lattice and the characteristics of the cell. In the second situation, the bandgap levels (conduction/valence band) are commonly disrupted [28]. Surprisingly, there is a size relationship between efficient bandgap energy and particle size of $ZnCr_2O_4$. The nanoparticle spinel structure, the particle sizes, and the monodispersed nanoparticles are easily detected from the SEM and TEM images. As a result, the varied fuel components can be a highly valuable and effective tool for controlling crystallite size and changing the magnetic characteristics of the produced nanoparticles.

3.4. VSM Hysteresis Loop Analysis. The magnetic characteristics of $ZnCr_2O_4$ nanoparticles are described by the VSM hysteresis loop. It is performed using a VSM with a power range from −10 to +10 kOe, as shown in Figure 8. All $ZnCr_2O_4$ nanoparticles exhibited a hysteresis loop and ineffective resolution which confirms superparamagnetic characteristics of

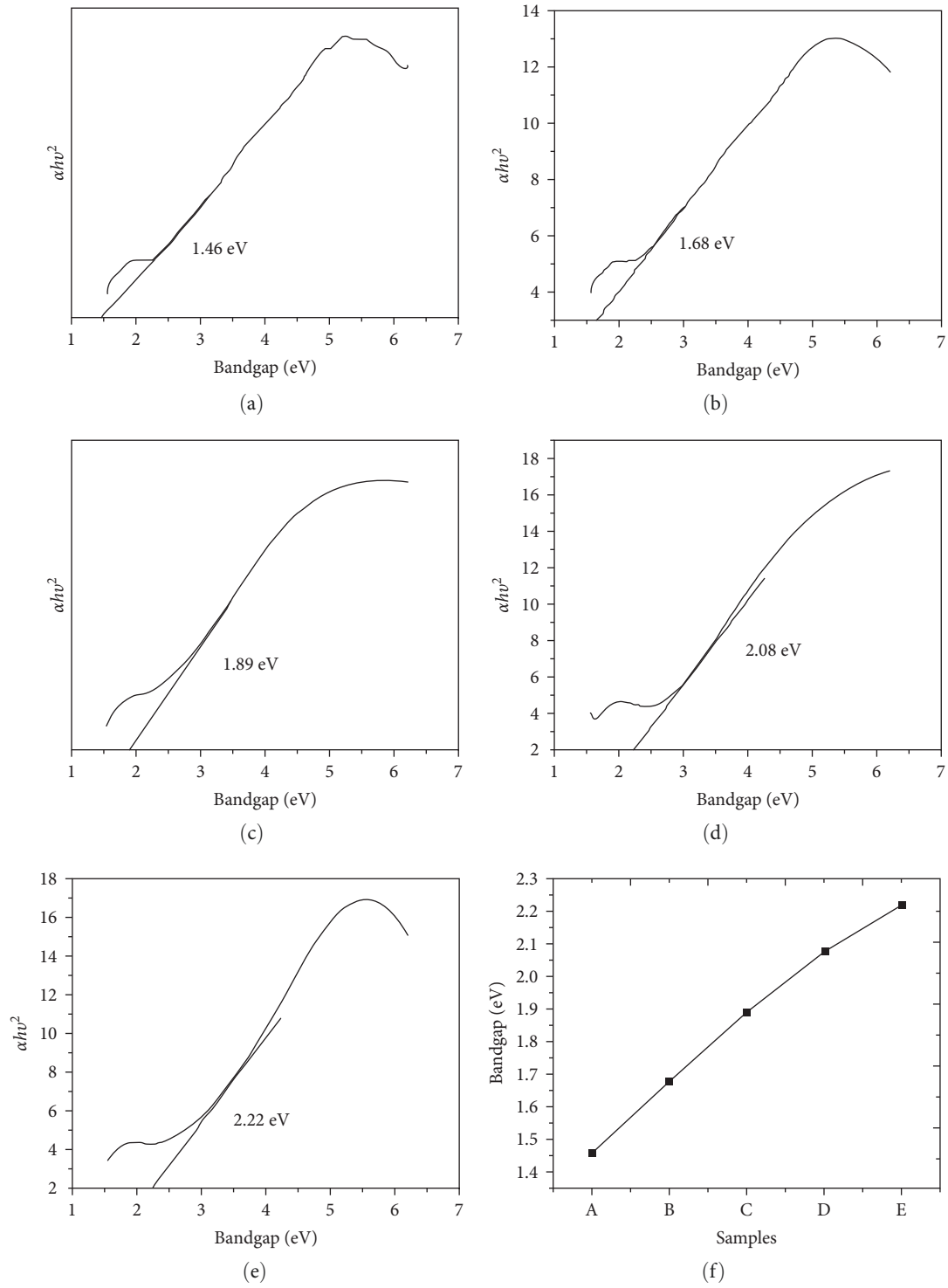

Figure 5: (a–e) Bandgap energy of $ZnCr_2O_4$ nanoparticles synthesized with five different fuels and (f) bandgap energy variation in $ZnCr_2O_4$ with respect to various fuels.

the as-synthesized nano-oxides. The magnetic hysteresis loops at ambient temperature demonstrate the behavior of ferromagnetic or superparamagnetic behavior of all $ZnCr_2O_4$ nanoscale samples. The magnetic parameters get tuned according to the difference in the proportions of the $ZnCr_2O_4$ nanometal oxides.

The total magnetic response of the pure and mixed metal oxide depends on the magnetic agent, volume fraction of metal oxides and the susceptibility of metal oxide (i.e., $ZnCr_2O_4$). The magnetic nature of Fe_3O_4 is generated by the Zn^{2+} cations because of the presence of the tetrahedral sites of the crystal lattice, and they also exhibit opposite

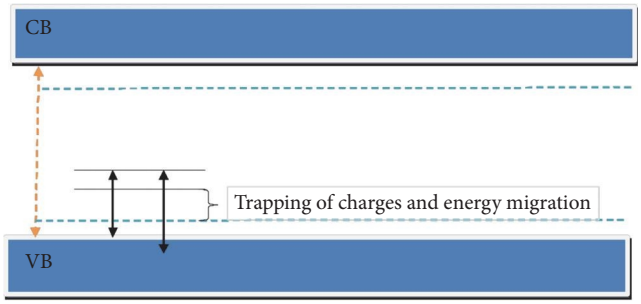

Figure 6: Bandgap energy trapping of charges and energy migration surface of $ZnCr_2O_4$.

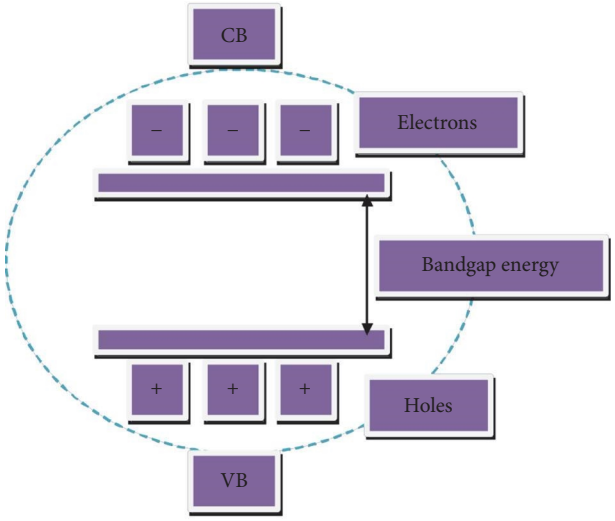

Figure 7: Energy levels between the VB and CB, electrons into holes reform of $ZnCr_2O_4$.

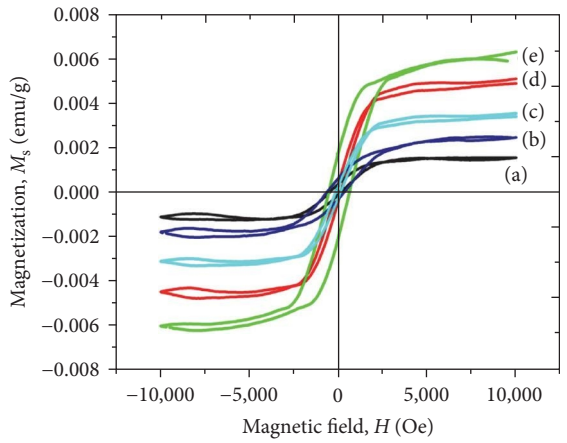

Figure 8: VSM spectra of $ZnCr_2O_4$ synthesized with various fuels.

results to one another. The octahedral site is oriented in the applied magnetic field direction, whereas the tetrahedral site is directed in opposition to the employed magnetic field; hence, the Zn^{3+} magnetic (Table 3) moments are neutralized. In the spinel structure, the tetrahedral positions are small as compared to the octahedral positions, and because of this, Cr^{3+} ions choose the octahedral B-position ions [29–32].

Table 3: Magnetic properties (magnetization, remanence, and coercivity) of nano $ZnCr_2O_4$ synthesized with various fuels.

$ZnCr_2O_4$ samples	H_c (Oe)	M_r (emu/g)	M_s (emu/g)
a	28.34	6.12	23.12
b	32.09	7.78	27.45
c	43.55	08.68	30.32
d	48.67	9.09	45.34
e	51.98	10.34	49.56

3.5. Solution Combustion Process. The solution combustion technique is a redox combustion process that produces nanoscale oxide powder. After finding the appropriate microwave power for production of nanocatalysts, the $ZnCr_2O_4$ nanoscale powder samples are synthesized with five different fuel types. When just the auxiliary fuel is employed for nanocatalyst production, the combustion is turned into a smoldering process with no visible flame. The smoldering combustion might cause two effects in this situation. At first, the combustion temperature and sintering of the sample are noticeably lowered, resulting in a lower intensity of the metal oxides peak. In reality, warming the final powder during sintering produced an egression of metal oxides cations from the alumina lattice, whereas the metal oxides cations are entirely diffused into the alumina lattice to create the spinel structure by utilizing fuels.

Second, because of the low temperature of the combustion media, just a few precursors are transformed from an amorphous to a crystalline state. The resulting nanoscale powder is the result of adequate breakdown of the precursor nitrate salts created by the low combustion temperature. This study exemplifies the nanocatalyst synthesis with the presence of combustion media that supplies necessary combustion heat to convert materials from nitrate to crystal form. It is possible to see the formation of a suitably uniform distribution of five fuel kinds into crystal on the surface of $ZnCr_2O_4$. The uniform distribution of particles on the surface may be obtained by increasing the quantity of fuel type, which could be the cause for the necessary solution temperature throughout synthesis [33, 34].

4. Conclusion

Nanoscale $ZnCr_2O_4$ has been synthesized by using the microwave combustion technology to investigate the chemical reaction impact of a series of five fuel molecules (citric acid, succinic acid, maleic acid, glycine, and urea) in a combustion reaction mechanism. The physicochemical investigations are carried out to confirm the structure, morphology, and composition. The XRD results reveal the formation of single-phase high pure $ZnCr_2O_4$. The easy fuel reduction in the regenerated mixture is occurred according to the modified stoichiometry of the direct reaction toward the mixed nitrate–fuel complex in the operating conditions. The heat emission is lower than expected from the stoichiometric

reaction, thus ending the direct reaction to $ZnCr_2O_4$ production. The mean particle size acquired from the HR-SEM approach is in concurrence with the mean particle size acquired from the X-ray line broadening method. A slight variation in the particle size might be due to the creation of aggregates. The lowest bandgap of $ZnCr_2O_4$ is found to be 1.46 eV for glycine fuel and the same could be tuned by using different fuels. All $ZnCr_2O_4$ samples show superparamagnetic behavior, which get tuned according to the difference in the proportions of the $ZnCr_2O_4$ nanometal oxides. The tunable optical and magnetic properties of $ZnCr_2O_4$ nanoparticles are suitable for optoelectronic device applications. Further studies on the antibacterial, photocatalyt, and catalyst mechanism are currently under investigation.

Data Availability

The data used to support the findings of this study are included in this article.

Conflicts of Interest

The authors declare that they have no conflicts of interest.

Funding

One of the corresponding authors (Dr. Gopal Ramalingam) acknowledges the financial support by MHRD-SPARC-890 (2019) and instrumentation facility utilized from RUSA 2.0 (grant no. F.24 51/2014-U), Policy (TNMultiGen), Government of India projects. The coauthor, Dr. Mohammed Mujahid Alam, specially thanks to the Deanship of Scientific Research, King Khalid University, Saudi Arabia, supported under grand number R.G.P.2/59/1443.

References

[1] C. Ragupathi, J. J. Vijaya, S. Narayanan, L. J. Kennedy, and S. Ramakrishna, "Catalytic properties of nanosized zinc aluminates prepared by green process using *Opuntia dilenii haw* plant extract," *Chinese Journal of Catalysis*, vol. 34, no. 10, pp. 1951–1958, 2013.

[2] C. Ragupathi, J. J. Vijaya, P. Surendhar, and L. J. Kennedy, "Comparative investigation of nickel aluminate ($NiAl_2O_4$) nano and microstructures for the structural, optical and catalytic properties," *Polyhedron*, vol. 72, pp. 1–7, 2014.

[3] J. Baxter, Z. Bian, G. Chen et al., "Nanoscale design to enable the revolution in renewable energy," *Energy & Environmental Science*, vol. 2, no. 6, pp. 559–588, 2009.

[4] M. B. Mahajan and P. A. Joy, "Evolution and magnetic characteristics of NiO-Ni$(OH)_2$ core-shell nanostructures," *Physical Chemistry Chemical Physics*, vol. 15, no. 48, pp. 20808–20812, 2013.

[5] C. Ragupathi, J. J. Vijaya, S. Narayanan, S. K. Jesudoss, and L. J. Kennedy, "Highly selective oxidation of benzyl alcohol to benzaldehyde with hydrogen peroxide by cobalt aluminate catalysis: a comparison of conventional and microwave methods," *Ceramics International*, vol. 41, Part A, no. 2, pp. 2069–2080, 2015.

[6] F. Gözüak, Y. Köseoğlu, A. Baykal, and H. Kavas, "Synthesis and characterization of $Co_xZn_{1-x}Fe_2O_4$ magnetic nanoparticles via a PEG-assisted route," *Journal of Magnetism and Magnetic Materials*, vol. 321, no. 14, pp. 2170–2177, 2009.

[7] Y. Köseoğlu, F. Alan, M. Tan, R. Yilgin, and M. Öztürk, "Low temperature hydrothermal synthesis and characterization of Mn doped cobalt ferrite nanoparticles," *Ceramics International*, vol. 38, no. 5, pp. 3625–3634, 2012.

[8] F. Cheng, Z. Peng, C. Liao et al., "Chemical synthesis and magnetic study of nanocrystalline thin films of cobalt spinel ferrites," *Solid State Communications*, vol. 107, no. 9, pp. 471–476, 1998.

[9] M. Sajjia, M. Oubaha, M. Hasanuzzaman, and A. G. Olabi, "Developments of cobalt ferrite nanoparticles prepared by the sol–gel process," *Ceramic International*, vol. 40, Part A, no. 1, pp. 1147–1154, 2014.

[10] K. C. Patil, S. T. Aruna, and S. Ekambaram, "Combustion synthesis," *Current Opinion in Solid State and Materials Science*, vol. 2, no. 2, pp. 158–165, 1997.

[11] C. Ragupathi, L. J. Kennedy, and J. J. Vijaya, "A new approach: synthesis, characterization and optical studies of nano-zinc aluminate," *Advanced Powder Technology*, vol. 25, no. 1, pp. 267–273, 2014.

[12] C. Ragupathi, J. J. Vijaya, and L. J. Kennedy, "Preparation, characterization and catalytic properties of nickel aluminate nanoparticles: a comparison between conventional and microwave method," *Journal of Saudi Chemical Society*, vol. 21, no. Supplement 1, pp. S231-S239, 2017.

[13] C. Ragupathi, J. J. Vijaya, and L. J. Kennedy, "Synthesis, characterization of nickel aluminate nanoparticles by microwave combustion method and their catalytic properties," *Materials Science and Engineering: B*, vol. 184, pp. 18–25, 2014.

[14] C. Ragupathi, J. J. Vijaya, R. T. Kumar, and L. J. Kennedy, "Selective liquid phase oxidation of benzyl alcohol catalyzed by copper aluminate nanostructures," *Journal of Molecular Structure*, vol. 1079, pp. 182–188, 2015.

[15] I. Khan, S. Khan, H. Ahmed, and R. Nongjai, "Structural and dielectric properties of Mn doped copper oxide (CuO) nanostructure," *AIP Conference Proceedings*, vol. 1536, no. 1, pp. 241-242, Article ID 241, 2013.

[16] G. K. Williamson and R. E. Smallman, "III. Dislocation densities in some annealed and cold-worked metals from measurements on the X-ray Debye–Scherrer spectrum," *The Philosophical Magazine: A Journal of Theoretical Experimental and Applied Physics*, vol. 1, no. 1, pp. 34–46, 1956.

[17] L. Li, C. Xiang, X. Liang, and B. Hao, "$Zn_{0.6}Cu_{0.4}Cr_{0.5}$-$Fe_{1.46}Sm_{0.04}O_4$ ferrite and its nanocomposites with polyaniline and polypyrrole: preparation and electromagnetic properties," *Synthetic Metals*, vol. 160, no. 1-2, pp. 28–34, 2010.

[18] S. Calvin, C. J. Riedel, E. E. Carpenter, S. A. Morrison, R. M. Stroud, and V. G. Harris, "Estimating crystallite size in polydispersed samples using EXAFS," *Physica Scripta*, vol. 2005, no. T115, Article ID 744, 2005.

[19] S. Gopinath, K. Sivakumar, B. Karthikeyen, C. Ragupathi, and R. Sundaram, "Structural, morphological, optical and magnetic properties of Co_3O_4 nanoparticles prepared by conventional method," *Physica E: Low-dimensional Systems and Nanostructures*, vol. 81, pp. 66–70, 2016.

[20] C. Ragupathi, J. J. Vijaya, L. J. Kennedy, and M. Bououdina, "Nanostructured copper aluminate spinels: Synthesis, structural, optical, magnetic, and catalytic properties," *Materials Science in Semiconductor Processing*, vol. 24, pp. 146–156, 2014.

[21] Y. Slimani, H. Güngüneş, M. Nawaz et al., "Magneto-optical and microstructural properties of spinel cubic copper ferrites with Li-Al co-substitution," *Ceramics International*, vol. 44, no. 12, pp. 14242–14250, 2018.

[22] X. Li, Y. Hou, Q. Zhao, and L. Wang, "A general, one-step and template-free synthesis of sphere-like zinc ferrite nanostructures with enhanced photocatalytic activity for dye degradation," *Journal of Colloid and Interface Science*, vol. 358, no. 1, pp. 102–108, 2011.

[23] A. A. Othman, M. A. Osman, E. M. M. Ibrahim, M. A. Ali, and A. G. Abd-Elrahim, "Mn-doped ZnO nanocrystals synthesized by sonochemical method: structural, photoluminescence, and magnetic properties," *Materials Science and Engineering: B*, vol. 219, pp. 1–9, 2017.

[24] D. Sharma and R. Jha, "Transition metal (Co, Mn) co-doped ZnO nanoparticles: effect on structural and optical properties," *Journal of Alloys and Compounds*, vol. 698, pp. 532–538, 2017.

[25] P. C. Patel, S. Ghosh, and P. C. Srivastava, "Unusual ferromagnetic to paramagnetic change and bandgap shift in ZnS: Cr nanoparticles," *Journal of Electronic Materials*, vol. 48, pp. 7031–7039, 2019.

[26] M. Ashokkumar and S. Muthukumaran, "Tuning of energy gap, microstructure, optical and structural properties of Cr doped $Zn_{0.96}Cu_{0.04}O$ nanoparticles," *Powder Technology*, vol. 258, pp. 157–164, 2014.

[27] J.-J. Miao, H. Wang, Y.-R. Li, J.-M. Zhu, and J.-J. Zhu, "Ultrasonic-induced synthesis of CeO_2 nanotubes," *Journal of Crystal Growth*, vol. 281, no. 2-4, pp. 525–529, 2005.

[28] M. D. Hernández-Alonso, A. B. Hungría, A. Martínez-Arias et al., "Confinement effects in quasi-stoichiometric CeO_2 nanoparticles," *Physical Chemistry Chemical Physics*, vol. 6, no. 13, pp. 3524–3529, 2004.

[29] F. Wallington, A. M. Arevalo-Lopez, J. W. Taylor et al., "Spin-orbit transitions in α- and $\gamma-CoV_2O_6$," *Physical Review B*, vol. 92, no. 12, Article ID 125116, 2015.

[30] M. Lenertz, A. Dinia, S. Colis et al., "Magnetic structure of ground and field induced ordered states of low-dimensional γ-CoV_2O_6," *The Journal of Physical Chemistry C*, vol. 118, no. 25, pp. 13981–13987, 2014.

[31] N. R. Wilson, O. A. Petrenko, and G. Balakrishnan, "Magnetic phase diagrams of the Kagomé staircase compounds $Co_3V_2O_8$ and $Ni_3V_2O_8$," *Journal of Physics: Condensed Matter*, vol. 19, no. 14, Article ID 145257, 2007.

[32] N. R. Wilson, O. A. Petrenko, and L. C. Chapon, "Magnetic phases in the Kagomé staircase compound $Co_3V_2O_8$ studied using powder neutron diffraction," *Physical Revew B*, vol. 75, no. 9, Article ID 094432, 2007.

[33] D. Dhak and P. Pramanik, "Particle size comparison of soft-chemically prepared transition metal (Co, Ni, Cu, Zn) aluminate spinels," *Journal of American Ceramic Society*, vol. 89, no. 3, pp. 1014–1021, 2006.

[34] D. Visinescu, B. Jurca, A. Ianculescu, and O. Carp, "Starch – a suitable fuel in new low-temperature combustion-based synthesis of zinc aluminate oxides," *Polyhedron*, vol. 30, no. 17, pp. 2824–2831, 2011.